Compression-Molded Polyurethane Block Copolymers. 1. Microdomain Morphology and Thermomechanical Properties

J. T. Koberstein,* A. F. Galambos,† and L. M. Leung‡

Department of Chemical Engineering and Institute of Materials Science, University of Connecticut, Storrs, Connecticut 06269-3136

Received October 3, 1991; Revised Manuscript Received July 6, 1992

ABSTRACT: The microdomain structure and thermomechanical properties of a series of compression-molded segmented polyurethane block copolymers are investigated as a function of hard-segment content. The crystallizable hard segments form from the reaction of 4,4′-diphenylmethane diisocyanate (MDI) with 1,4-butanediol (BDO). Soft segments are poly(oxypropylene) end-capped with poly(oxyethylene). Polyurethanes containing 40% or less by weight of hard segment exhibit a discrete hard-segment morphology. Materials with higher amounts of hard segment show hard-segment microdomain structures consistent with the lamellar model of Koberstein and Stein. Melting behavior is found to be rate dependent, reflecting kinetic effects on microdomain structure during thermal cycling. At high heating rates, DSC thermograms exhibit a single high-temperature endotherm corresponding to the melting of an extended form of a MDI/BDO crystal. Multiple endotherms are observed at low DSC scan rates. For high hard-segment content specimens, catastrophic softening is coincident with the onset of the first high-temperature endotherm. The primary softening point for materials with discrete hard microdomains occurs at the soft microphase T_g. The soft microphase T_g is a minimum for a hard-segment content of 50%. The apparent hard microdomain T_g decreases monotonically with increasing hard-segment content and is consistent with heat capacity data for the soft microphase T_g which indicates increased incorporation of soft-segment material into the hard microdomain for higher hard-segment content materials. Small-angle X-ray scattering measurements of the specific interfacial area and estimates of the lamellar thickness suggest that the critical hard-segment length corresponds to a chain with 3–4 MDI residues. In this model, hard segments that are shorter than the critical length are assumed to be dissolved within the soft microphase. The degree of microphase separation generally improves with an increase in the hard-segment content, correlating well with the corresponding decrease in the fraction of hard segments of length below the critical length. Intersegmental mixing occurs primarily within the microphase; only a minor fraction of the mixing occurs within the diffuse microphase interphase.

I. Introduction

Segmented polyurethane elastomers are copolymers with $-[(s)_n(h)_m]-_p$ type chain architecture where s and h are the soft- and hard-segment sequences, respectively. The soft segment is typically an oligomeric rubber at use temperature, while the hard segment is either a glassy or crystalline material under these conditions. Due to thermodynamic differences, the segments usually segregate to form an aggregated pseudo-two-phase structure. The structure formed is limited by the short length of the segments to assume microscopic dimensions and is thus termed the microdomain structure. As a result of their small size, the hard-segment microdomains act as extremely efficient fillers and provide physical cross-link sites for the soft microphase. Interesting properties similar to those of triblock copolymer elastomers are often obtained.

Considerable academic and industrial effort has focused on elucidating the structure–property relationships in segmented polyurethanes as a result of their versatility in a broad range of applications. Polyurethanes containing crystallizable hard segments comprised of a diphenylmethane diisocyanate (MDI) chain extended with 1,4-butanediol (BDO) have been studied most extensively. A central theme in these studies has been the development of a structural model for the internal hard microdomain structure, based primarily on the results of small-angle X-ray scattering[1–8] and X-ray diffraction[3,4,7,9–18] studies. Complementary studies using dynamic mechanical and thermal[17,19–32] analysis methods have furnished additional information on glass transition temperatures and microphase purity and have documented the general behavior of high-temperature multiple endotherms[18,28,30] in these polyurethanes. Although much information has been gathered about polyurethane structure and properties, relatively little progress has been made in constructing quantitative structure–property correlations for segmented polyurethanes.

In this series of papers we present a comprehensive study of correlations between thermal and thermomechanical properties, thermal history, microdomain structure, and microphase mixing in segmented polyurethanes prepared from MDI, BDO, and poly(propylene oxide–ethylene oxide) (PPO–PEO) soft segments. These materials have already been subject to extensive analysis in our laboratories using a wide range of techniques including small-angle X-ray scattering,[6,33] thermal analysis,[7,33,34] solid-state deuterium NMR,[35,36] simultaneous differential scanning calorimetry (DSC)/synchrontron X-ray scattering,[33] and Fourier transform infrared spectroscopy.[37] This first paper in the series deals with correlations between thermal and thermomechanical properties.

Thermoanalytical techniques have provided a broad base of information on MDI/BDO-based polyurethanes. Bonart et al.[9–11] used different heat treatments to prepare specimens with either paracrystalline or true crystalline order. X-ray diffraction results were used to construct possible hard-segment packing models based upon consideration of the formation of a physical cross-linking network of interurethane hydrogen bonds. DSC characterization revealed apparent melting endotherms for both materials but a substantially higher melting temperature for the crystalline material. The small-angle X-ray scattering profiles and heat distortion temperatures were

* To whom correspondence should be addressed.
† Present address: Himont Research and Development Center, 800 Greenbank Road, Wilmington, DE 19808.
‡ Present address: Department of Chemistry, Hong Kong Baptist College, 224 Waterloo Road, Kowloon, Hong Kong.

0024-9297/92/2225-6195$03.00/0

also found to differ for the two materials, but structure–property correlations could not be made. Heat distortion in the paracrystalline material was associated with melting and dissociation of the physical cross-link network; however, heat distortion occurred some 30 °C below the melting point in the crystalline material.

Low-temperature softening was found to occur at the soft microphase T_g, at temperatures above that of the pure soft-segment T_g, due to the presence of disordered hard segments distributed within the soft matrix. High-temperature softening has not been attributed to any single transition but has been reported to occur over a range of temperatures where multiple endotherms are observed.[9,10,20] These multiple endotherms are sensitive to the annealing history and are not thoroughly understood at present. X-ray diffraction studies[39-41] have demonstrated that multiple endotherms in highly-oriented heat-set materials are correlated with transformations between extended and contracted hard-segment crystalline polymorphs. Simultaneous SAXS–DSC experiments[33] have shown that partial disordering of the hard microdomains occurs during each of the endotherms consistent with the softening behavior. Above the crystalline melting point, these polyurethanes disorder completely.

The thermal transitions in polyurethanes are directly related to the state of mixing between the hard and soft segments. The shorter hard segments can dissolve within the soft microphase if their length is below the critical length for microphase separation. This dissolution process elevates the soft microphase glass transition temperature and degrades the material's low-temperature response. Soft segments may also dissolve into the hard microdomains or become trapped therein during structure formation. Mixing of this nature decreases the resistance of the hard microdomain to plastic flow, leading to a decrease in the heat distortion temperature. A detailed, morphological model of a hard microdomain structure is required if the relationships between these material properties and the molecular architecture are to be understood.

Previous publications[5,6] reviewed many of the models that have been proposed for polyurethane hard segments based upon the reaction of BDO and MDI. A detailed morphological analysis[6] of a series of these materials using small-angle X-ray scattering (SAXS) showed that the hard microdomain structure was in qualitative agreement with a model proposed by Koberstein and Stein.[5] The basis of this model is partial solubilization of short hard segments into the soft microphase. Hard segments shorter than the critical length for microphase separation are presumed to remain within the soft microphase while longer segments aggregate into lamellar hard microdomains of thickness proportional to the critical sequence length. Models of this nature provide a means for relating chemical structure and thermodynamics to the properties of polyurethanes.

In what follows, we describe the thermoanalytical and structural characterization of a set of compression-molded polyurethane specimens differing in hard-segment content. The conditions of molding have been selected to provide a simplified morphology that is characterized by a single hard-segment melting point. The results of this characterization are used to investigate correlations between thermal and mechanical transitions (i.e., soft and hard microphase glass transitions, heat distortion temperatures, multiple endotherms, and softening points) as well as their morphological origins.

Table I
Characteristics of Specimens

materials	hard segment (wt %) (MDI + BDO)	density (g/cm³)	no. av MW[a] of hard segment (g/mol of HS)	hard segment theor vol fraction
PU-20	20	1.142	500	0.17
PU-30	30	1.165	800	0.26
PU-40	40	1.192	1200	0.35
PU-50	50	1.218	1700	0.45
PU-60	60	1.235	2300	0.55
PU-70	70	1.270	3100	0.66
PU-80	80	1.292	4300	0.77

[a] Calculated from the most probable distribution for a one-step polymerization.

II. Experimental Materials

The materials studied are a series of segmented polyurethane block copolymers with varying hard-segment content, denoted PU–*XX*, where *XX* represents the weight percent of hard segment units in the material. Hard segments consist of a 4,4′-diphenylmethane diisocyanate chain extended with 1,4-butanediol, while the soft segment is poly(oxypropylene) (PPO, $\bar{M}_n$ = 2000, functionality = 1.94) end-capped with 30.4 wt % poly(oxyethylene) (PEO). The polymers were prepared by a one-step polymerization with 4% excess MDI to ensure complete reaction, as described in the literature.[24] Chemical compositions of the materials as well as some related physical properties are presented in Table I. In addition to these materials, a hard-segment end-capped polyol prepolymer, PU15, was prepared as a model polymer. Its properties are important to analyses that appear in later papers in this series. Specimens employed in this study have been reprecipitated from dimethylformamide solutions of the "as-received" polymers,[42] vacuum dried, and molded into 2-mm-thick, 1.5-in.-diameter disks at 180 °C and 3000 psi pressure for 5 min under vacuum. These conditions were selected because they yielded materials which exhibit only a single melting endotherm (for high DSC heating rates), thus implying the existence of relatively simple morphologies compared to specimens exhibiting multiple endotherms. The chemical content of a selected molded specimen was verified as equivalent to that of the as-received polymer by elemental analysis. In addition, the solubility behavior of the material was unchanged by molding, and thermal properties were found to be reproducible upon thermal cycling. On the basis of this evidence, we conclude that there is not any significant degradation of our specimens during molding, at least to any level which influences our results at present.

Differential Scanning Calorimetry. DSC data for all of the copolymers and the pure soft-segment prepolymer were obtained with a Perkin-Elmer DSC-4 equipped with a Model 3600 data station and calibrated with indium, cyclohexane, and sapphire standards. Characterization of the low-temperature behavior of the specimens was accomplished by scanning at a rate of 20 °C/min from −140 °C to room temperature. Measurements were repeated 10–15 times with fresh samples each time in order to establish statistical error limits on the values of the glass transition temperature (T_g) of the soft microphase and the change in heat capacity (ΔC_p) at the transition.

Thermal behavior above room temperature was investigated by scanning the specimens from 20 to 240 °C at scan rates of 20 and 40 °C/min. Values of peak maximum and onset temperatures, as well as fusion enthalpies of apparent hard-segment melting endotherms, are reported.

Thermomechanical Analysis (TMA). Molded specimens were subjected to flexure and penetration probe analysis using a Perkin-Elmer thermomechanical analyzer (TMA-LO). Flexure tests were performed with an applied load of 66 psi at a scan rate of 5 °C/min. Specimens were mounted on a quartz cantilever platform and scanned over two temperature ranges: −100 to +50 °C, for detection of the soft microphase deflection point, and 30 to 170 °C, for detection of the hard microdomain deflection temperature. The reported transition temperatures are the intersections of tangents drawn to the probe position versus temperature curve before and during deflection. Penetration

probe tests were run on the molded materials with a probe load of 10 g and were scanned from 0 to 220 °C at a rate of 20 °C/min. All reported transition temperatures were calibrated to the softening temperature of indium. As with the flexure studies, transition temperatures were taken as the intersection of tangents drawn to the probe position versus temperature curve in the region of interest.

Wide-Angle X-ray Scattering (WAXS). Wide-angle X-ray scattering (WAXS) profiles of the molded disks were collected in the reflection mode using a Philips goniometer. Nickel-filtered Cu Kα radiation (wavelength = 0.1542 nm) was produced by an XRG-3000 generator at an operating voltage of 40 kV and a current of 20 mA. The scattering intensity was monitored on a strip-chart recorder as a function of the scattering angle (2θ) between 5 and 35° using a goniometer arm speed of 1°/min.

Small-Angle X-ray Scattering (SAXS). Small-angle X-ray scattering experiments were performed at the AT&T Engineering Research Center in Princeton, NJ, using a step-scanning Kratky camera equipped with a proportional counter. The source of Cu Kα X-rays gave a wavelength of 1.54 Å when filtered through nickel foil. The sample-to-detector distance was 214 mm, the step size was 50 μm, and the accumulation time was 60 or 200 s. The camera was aligned for infinite slit optics using a 60-μm entrance slit and a 150-μm receiving slit. Absolute intensity calibration was accomplished with a Lupolen standard. The raw intensity curves were smoothed,[42] corrected for parasitic slit scattering and sample attenuation, and desmeared according to the method of Vonk.[43] Details of these procedures have been reported elsewhere.[6,42,44]

SAXS Analysis. The small-angle X-ray scattering technique provides a convenient means for evaluating morphological details of materials with heterogeneities in the 1–100-nm size range. The experiment involves measurement of the scattered intensity as a function of the angle measured with respect to the direction of the incident X-ray beam. The direction of the scattered radiation is usually expressed in terms of the scattering vector, s, defined by

$$s = 2 \sin (2\theta/2)/\lambda \tag{1}$$

where λ is the X-ray wavelength and 2θ is the scattering angle. If a relative maximum is observed in the scattering intensity at a particular scattering vector, s_{max}, the size (i.e., wavelength), d, of the periodic structure from which this interference arises may be approximated through Bragg's law

$$d_{3D} = 1/s_{max} \tag{2}$$

For one-dimensional scattering systems which are globally isotropic (i.e., randomly oriented lamellar stacks) this relation becomes

$$d_{1D} = 1/s'_{max} \tag{3}$$

where s'_{max} is the scattering vector corresponding to a maximum in the quantity $I(s)\,s^2$. $I(s)$ is the scattered intensity, and d_{1D} is the one-dimensional interlamellar repeat distance.

The scattering intensity arises due to local heterogeneities in the electron density of the material. For a two-phase system, the intensity at any scattering vector may be expressed as

$$I(s) \sim \bar{\eta}^2 \int_0^\infty \gamma(r)\, e^{-i(2\pi r \cdot s)}\, dr \tag{4}$$

where $\gamma(r)$ is the correlation function. The correlation function for a lamellar structure will have a local maximum at a position r which corresponds to the interlamellar repeat distance, d_{1D}. This correlation function, $\gamma_{1D}(r)$, is defined in terms of the fluctuation, $\eta(r)$, from the average electron density at position r

$$\gamma(r) = \frac{\langle \eta(0)\, \eta(r) \rangle}{\bar{\eta}^2} \tag{5}$$

where 0 represents an arbitrary origin. The term $\bar{\eta}^2$ is the mean-squared fluctuation in electron density and serves as a measure of the completeness of the microphase separation. For a two-phase system it is equivalent to

$$\bar{\eta}^2 = \phi_1 \phi_2 (\rho_1 - \rho_2)^2 \tag{6}$$

where ρ_i and ϕ_i denote the electron density and volume fraction of each phase, respectively. The magnitude of $\bar{\eta}^2$ can be determined by rearrangement and integration of the scattering relation (4). The correlation function is calculated by applying an inverse Fourier transform to the scattering relation for the experimental scattering profile.[5,6,42,44]

The integrations and transforms involved in calculating these structural parameters require extrapolation to an infinite scattering vector. The extrapolation is accomplished through the application of Porod's law

$$\lim_{s \to \infty} [I(s)] = K_p/s^4 \tag{7}$$

Porod's law constant is related to the surface-to-volume ratio, S/V, by the relation

$$K_p = 2\pi i_e \bar{\eta}^2 (S/V) \tag{8}$$

with i_e the Thompson scattering factor for a single electron.

Intraphase mixing and diffuse microphase boundaries lead to deviations from Porod's law[45-47] which may be analyzed to estimate their respective contributions to the overall mixing. In the case of collimation by infinitely long slits, a modified Porod's law results in

$$\lim_{s \to \infty} [\tilde{I}(s)] = \frac{\tilde{K}_p}{s^3} \tilde{H}^2(s) + \tilde{I}_B(s) \tag{9}$$

The slit smeared intensity, $\tilde{I}(s)$, contains a background contribution, $\tilde{I}_B(s)$, arising from both the thermal density and concentration fluctuations. The background may be considered a constant under certain conditions[1,2] and can be evaluated by a plot of $\tilde{I}(s)\,s^3$ against s^3.

The presence of diffuse phase boundaries damps out the limiting Porod intensity by the factor $\tilde{H}^2(s)$. When the interphase concentration profile is sigmoidal in nature, the damping function may be approximated by[4,5]

$$\tilde{H}^2(s) = \exp[-38(\sigma s)^{1.81}] \tag{10}$$

An equivalent thickness, E, for a linear interphase gradient is given by $E = 12^{1/2}\sigma$, where σ is the half-width of the Gaussian smoothing function used to generate the sigmoidal interphase profile. The value of σ is obtained[46] from analysis of a graph of the quantity $\ln \{[\tilde{I}(s) - \tilde{I}_B(s)]s^3\}$ against $s^{1.81}$. The value of the Porod constant, $\tilde{K}_p$, can be used to determine S/V using a relation[6] similar to (8).

In the limit of the infinite slit length assumption two variances may be calculated. A variance reflecting the overall degree of microphase separation is

$$\overline{\Delta\rho^{2'}} = C \int_0^\infty [\tilde{I}(s) - \tilde{I}_B(s)]\, s\, ds \tag{11}$$

while the variance defined as

$$\overline{\Delta\rho^{2''}} = C \int_0^\infty \frac{[\tilde{I}(s) - \tilde{I}_B(s)]s}{\tilde{H}^2(s)}\, ds \tag{12}$$

corrects for the effects of diffuse microphase boundaries.

A third ideal variance for complete microphase separation, $\overline{\Delta\rho_c^2}$, is furnished by (6), substituting in the pure component electron densities and volume fractions calculated from the known chemical composition.

III. Results

Subambient DSC. Low-temperature DSC behavior of the molded materials is typified by a single transition

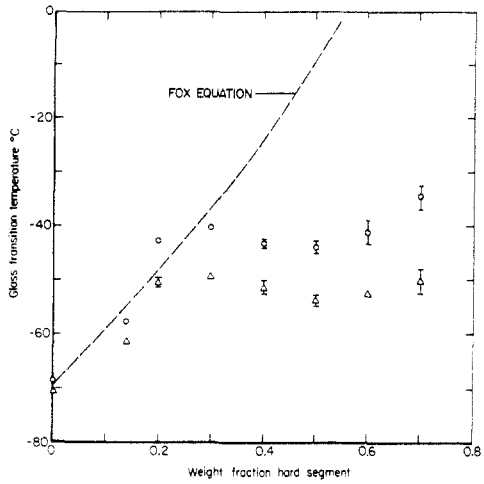

Figure 1. Soft microphase glass transition temperatures as a function of composition. The triangles represent T_g onset temperatures while the circles indicate midpoint T_g values. The dashed line represents the behavior (i.e., T_g midpoints) expected for homogeneous specimens in the absence of microphase separation.[34]

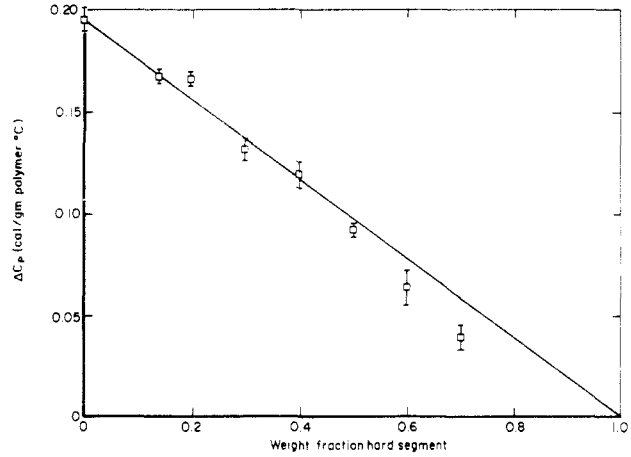

Figure 2. Change in specimen heat capacity at the soft microphase T_g as a function of sample composition.

corresponding to the glass-to-rubber transition of the soft microphase. As the hard-segment content of the specimens increases, the breadth of the transition region increases, while the magnitude of the observed change in heat capacity (ΔC_p) at the transition decreases, to the point of being indiscernable for the material containing 80 wt % hard segment.

Onset and midpoint values of the soft microphase glass transition temperatures are reported as a function of sample composition in Figure 1. The dotted line represents a modified Fox relationship[48,49] for the T_g's of homogeneous copolymer systems that was reported in a previous study[34] (i.e., systems in which there is complete intersegmental mixing). Deviation of the experimental values of T_g from the Fox prediction occurs at hard-segment weight fractions above 0.3, indicating a transition between a homogeneous and microphase-separated morphology at this composition. As the hard-segment content increases beyond this critical value, the soft microphase T_g decreases to a local minimum for 50% hard segment.

The magnitude of the change in heat capacity at the soft microphase glass transition decreases monotonically with increasing hard-segment content (see Figure 2 and Table II). For all materials except PU-20 the measured ΔC_p is equal to or less than that for complete microphase separation[34] (denoted by the solid line in Figure 2). The tendency for specimens with a higher hard-segment

Table II
Soft Microphase Glass Transition Data

specimen	glass transition DSC onset	glass transition DSC midpoint	ΔC_p (cal/g °C)	TMA flexure point (°C)
polyol	−71	−69	0.196	
PU-20	−51	−43	0.166	−45
PU-30	−50	−41	0.131	−42
PU-40	−52	−44	0.119	−44
PU-50	−54	−44	0.092	−40
PU-60	−53	−42	0.064	−37
PU-70	−51	−35	0.039	

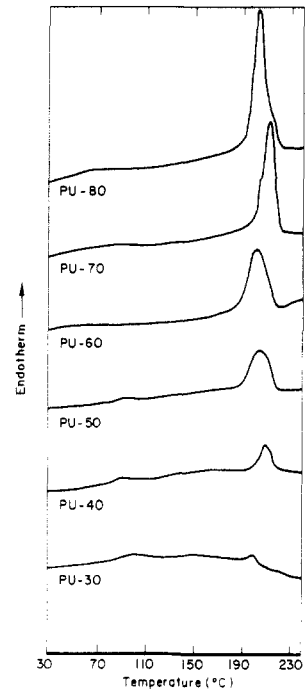

Figure 3. High-temperature DSC of molded samples. Scan rate of 40 °C/min.

Table III
High-Temperature Endotherm Temperatures (°C)

specimen	DSC onset[a]	DSC peak[a]	DSC onset[b]	DSC peak 1[b]	DSC peak 2[b]	TMA softening point[b]
PU-30	187	199	172	196	214	140
PU-40	200	207	198	207	222	172
PU-50	189	202	190	202	212	196
PU-60	189	201	190	201	214	195
PU-70	200	212	200	206	215	203
PU-80	194	204	196	205	219	199

[a] 40 °C/min. [b] 20 °C/min.

content to exhibit ΔC_p values below the ideal value indicates that some soft-segment units are incorporated within the hard microdomain and interphase regions and do not participate in the soft microphase glass transition process. This tendency is strongest for formulations with high hard-segment content.

High-Temperature DSC. DSC scans were also performed on the molded specimens over a temperature range of 0–240 °C. At scan rates of 40 °C/min (Figure 3) specimens exhibit a single high-temperature peak, in some cases accompanied by a smaller endotherm that exists as a high-temperature "shoulder" on the main peak (Table III). At a scan rate of 20 °C/min (Figure 4), however, all compositions with a hard-segment content above 40% exhibit distinct multiple endotherms. For these compression-molded materials simultaneous wide-angle X-ray diffraction/DSC experiments[44,50] indicate that the multiple

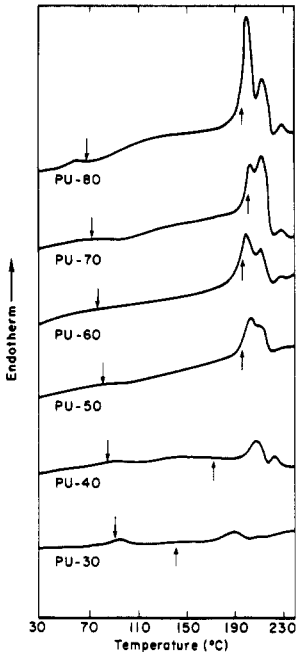

Figure 4. High-temperature DSC of molded samples. Scan rate of 20 °C/min. Down-arrows denote the onset of the initial transition in the penetration probe position; up-arrows signify the onset of catastrophic softening determined by penetration probe analyses performed at the same scan rate.

Table IV
Fusion Enthalpy and Apparent Crystallinity

	heat of fusion (DSC) (cal/g)		apparent % crystallinity (WAXS)	
specimen	polymer	hard segment[a]	polymer	hard segment[a]
PU-30	0.4	1.3	0	0
PU-40	1.5	3.8	3.7	9.3
PU-50	3.2	6.4	7.2	14.4
PU-60	4.8	8.0	9.3	15.5
PU-70	6.6	9.4	15.5	22.1
PU-80	8.2	10.3	13.4	16.7

[a] Assuming complete microphase separation.

endotherms result from melting and immediate melt recrystallization of extended MDI/BDO crystals.[39,40,52] Since multiple endotherms result from melt recrystallization during the DSC scan, we consider the 40 °C/min data to be most appropriate to our analyses.

The total enthalpy of the single high-temperature endotherms apparent in the 40 °C/min data (Figure 3) increases linearly with the hard-segment weight fraction (Table IV) to an extrapolated enthalpy of ca. 11.5 cal/g for the pure hard segment. A value of 22.5 cal/g has been reported for a model compound containing three MDI residues exhibiting a similar melting temperature (208 °C).[38]

Specimens with hard-segment contents of 30% and above exhibit an apparent glass transition process that occurs in the range of 50–90 °C (Table V). The transition is manifest as a small peak or change in slope of the DSC base line. Previous DSC annealing studies on polyurethanes[27,28,30,34] have also reported a weak endotherm of this nature, which has been referred to as an "annealing" or "room temperature annealing" peak, since it generally occurs about 20 °C above the annealing temperature, T_a. Its origin, however, has been ascribed to short-range ordering of the hard segments.

Several reasons lead us to believe that, in the present case, the small transition apparent in the 50–90 °C range for our compression-molded specimens reflects a hard microdomain T_g process. First of all, the specimens have been held at room temperature for an extended time period; the transitions occur at a temperature some 40–80 °C higher. Previous annealing (i.e., melt crystallization) studies[34] gave peak melting temperatures, T_p, that were ca. 20 °C above T_a. Furthermore, $T_p - T_a$ was previously found to be an increasing function of the hard-segment content, whereas T_p for the molded specimens is a decreasing function of the hard-segment content. As the DSC scan rate increases, the magnitude of the apparent peak diminishes and the transition assumes a more sigmoidal appearance typical of a glass transition. The shape of the low scan rate data is consistent with what would be expected if the glass transition were followed immediately by a recrystallization exotherm. The overall shape would be sigmoidal, followed by an exotherm, which has an appearance similar to that of a small endotherm. At higher rates, the recrystallization would be at a minimum such that the sigmoidal shape characteristic of T_g would be predominant. The appearance of this feature is further emphasized by the apparent skewness of the endotherm due to the slow cooling process. Additional crystallization during slow cooling is only possible until the temperature reaches T_g, below which there can be no melting endotherm. This effect also tends to produce an apparent transition near T_g. The behavior is fully consistent with what is observed experimentally, and thus we conclude that the DSC transitions found in the 50–90 °C range are reflective of an apparent hard microdomain T_g process. TMA results that follow also support this conclusion.

Table V
Apparent Hard Microdomain Glass Transition Temperatures (°C)

	TMA		
specimen	flexure probe[a]	penetration probe[b]	DSC peak[b]
PU-30		91	92
PU-40	72	83	87
PU-50	60	82	86
PU-60	46	78	77
PU-70	46	73	70
PU-80	47	70	61

[a] Scan rate of 5 °C/min. [b] Scan rate of 20 °C/min.

Values for the apparent ΔC_p and T_g midpoint for pure hard-segment specimens quenched from the melt were determined by DSC to be 0.09 cal/g °C and 112 °C (108 °C onset), respectively. It is not possible to determine quantitative ΔC_p values for the apparent hard microdomain glass transition of the molded polyurethanes; however, they are considerably smaller than would be calculated from the pure hard-segment values. This is expected due to the presence of some degree of hard-segment microcrystallinity and ordering and as a result of inclusion of hard segments within the soft microphase as discussed earlier.

Thermomechanical Analysis: Flexure Testing. Mechanical flexure tests were performed to determine heat distortion temperatures for each of the molded specimens. Distinct flexure occurred in specimens of low hard-segment content in temperature regions corresponding to both the hard and soft microphase glass transitions.

In the case of PU-20 and PU-30, the flexure of the cantilevered specimens was catastrophic at the low-temperature glass transition, reflecting the lack of a well-developed, discrete hard-segment domain morphology. The onset of low-temperature flexure was in all cases coincident with observed DSC values for the soft microphase T_g (see Table II).

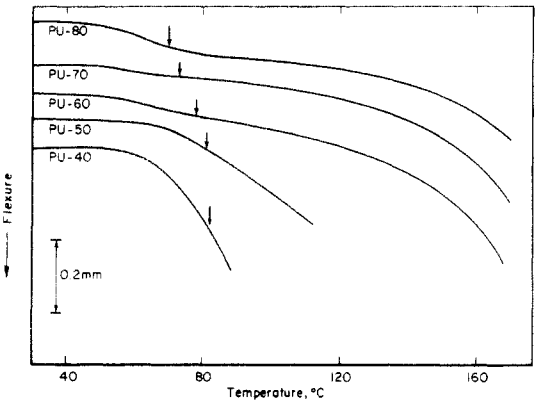

Figure 5. TMA of molded samples: High-temperature flexure probe; scan rate of 5 °C/min. Arrows indicate hard microdomain T_g values from penetration probe analysis (scan rate of 20 °C/min).

The flexure probe scan of PU-40 shows two distinct heat distortion temperatures observed in the vicinity of the hard (Figure 5) and soft microphase glass transition regions. This behavior is indicative of the development of a discrete hard microdomain structure within a soft microphase matrix.

Materials with hard-segment contents of 50% and greater do not exhibit appreciable flexure in the region of the soft microphase glass transition. Such behavior is consistent with the onset of a continuous hard microdomain structure at hard-segment contents of 50%, as was suggested by the results of SAXS analyses.[6]

High-temperature flexure curves are shown in Figure 5. The heat distortion temperature (i.e., onset of flexure) for PU-50 occurs at ca. 60 °C and is coincident with the onset of the apparent hard microphase glass transition. For specimens of higher hard-segment content, a softening point is also detectable at the apparent hard microphase T_g (Table V); however, catastrophic distortion does not take place until much higher temperatures, near 160 °C. Wide-angle X-ray scattering measurements that follow indicate that significant hard-segment crystalline or paracrystalline order develops in these latter materials. If the crystalline microdomain structure is continuous, heat distortion is expected to be minimal until the three-dimensional network of ordered hard-segment regions is disrupted at its melting temperature.

Thermomechanical Analysis: Penetration Probe Testing. Typical penetration probe scans on the molded specimens appear in Figure 6. For all specimens two transition points are noted in the region between room temperature and 240 °C: a change of slope in the probe position vs temperature scan between 60 and 80 °C and complete penetration of the probe as the specimens soften at higher temperatures. Cohen and Ramos[51] found similar penetration behavior for isoprene–butadiene block copolymer systems. They ascribed the lower temperature transition to the hard microphase glass transition. Similar TMA and DSC results for the polyurethane specimens support this conclusion. In addition, Cohen and Ramos observed a distinct transition in penetration probe behavior as the hard microdomain structure changed from discrete to continuous with increasing hard-segment content. For materials with discrete hard microdomains the slope of the penetration probe position vs temperature plot decreases at the T_g of the hard microphase (Figure 6). In contrast, an increase in the slope is observed for materials exhibiting continuous hard microdomain structures. Apparent hard microdomain glass transition temperatures are reported in Table V and compared to values

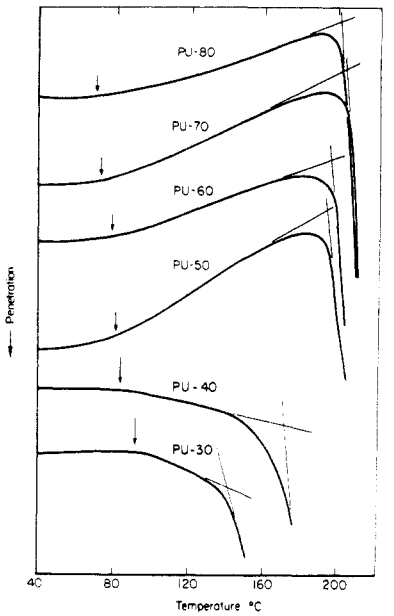

Figure 6. TMA of molded samples. High-temperature penetration probe; scan rate of 20 °C/min. Arrows indicate inflection points in the slope of the probe position vs temperature plot.

obtained from DSC and flexure probe analysis. The apparent hard microdomain T_g's from penetration probe analysis are systematically higher than those evaluated from the flexure analysis, as indicated on Figure 5 and in Table V. This is to be expected since the penetration probe data was taken at 20 °C/min compared to 5 °C/min for the flexure data. The DSC and penetration probe values were obtained from data collected at identical rates and are in reasonable agreement. The transition between discrete and continuous hard microdomain morphology is indicated to occur between 40 and 50 wt % hard segment for both flexure and penetration probe test data.

Softening behavior provides another basis for determination of the compositional transition in domain morphology. Specimens with hard-segment contents of 40% and less soften at considerably lower temperatures than specimens of higher hard-segment content. Additionally, for these compositions softening occurs at temperatures well below the high-temperature endotherms observed by DSC, indicating that hard-segment ordering does not provide significant structural reinforcement for these low hard-segment content polyurethanes at elevated temperatures. For specimens with a hard-segment weight content of 50% and above, however, softening is coincident with the onset of high-temperature DSC endotherms (Figure 4), supporting the evidence from flexure testing that these high hard-segment content molded specimens maintain mechanical integrity up to temperatures corresponding to the disruption of hard-segment aggregates.

Wide-Angle X-ray Scattering (WAXS). WAXS profiles of the molded specimens (Figure 7) are typified by a broad, amorphous scattering halo between 10 and 30° of 2θ accompanied by diffuse crystalline scattering peaks for samples with a higher hard-segment content. Comparison of the location of these peaks with literature values[4,12,13,39,52,53] indicates that the crystal form evident in the molded materials most closely matches that of the extended MDI/BDO crystal termed type I by Briber and Thomas.[39,52] Estimates of the fraction of crystallinity in each of the samples were obtained from WAXS analysis by comparing the area under the amorphous halo to the area under the crystalline peaks by the method outlined by Alexander[54] for semicrystalline polymers. The frac-

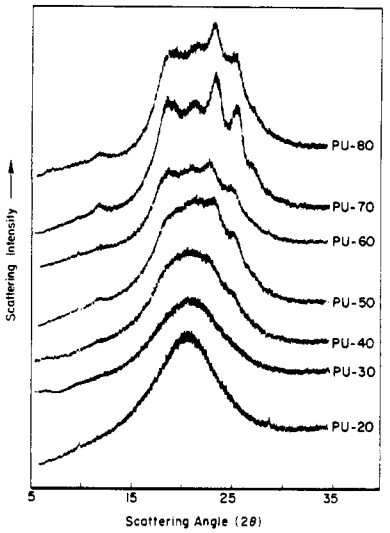

Figure 7. Wide-angle X-ray scattering profiles of molded specimens.

tional crystallinities (from WAXS analysis) based on the mass of polymer and the mass of hard segment are presented with similarly based hard-segment heats of fusion (from DSC analysis) in Table IV. The enthalpy of the single high-temperature DSC endotherm varies linearly with the hard-segment content, while the fractional crystallinity does not, reaching a maximum for PU-70 and actually decreasing for PU-80.

These trends are difficult to interpret directly for a number of reasons. First of all, the average hard-segment length and the distribution of hard-segment lengths change markedly with hard-segment content (see Table I). Previous studies on model hard segments[38] have shown that the heat of fusion is dependent on the hard-segment length. It is doubtful that the model compounds and the polyurethane hard segments crystallize in an identical fashion, but there, nonetheless, may be an effect of length (i.e., overall hard-segment content) on the heat of fusion. In addition, there is no direct way to quantitatively estimate the degree of crystallinity by traditional WAXS analysis of these materials due to an inability to measure an appropriate amorphous halo. When the hard segments melt, they also undergo an order–disorder transition and spontaneously mix intimately with the soft segments.[33] The amorphous halo of this melt state is significantly different from that of a noncrystalline microphase-separated material.[44] The latter WAXS pattern is the appropriate one to employ in the crystallinity calculation but is generally unobtainable experimentally. The reported crystallinities are based upon the WAXS of the disordered melt and therefore cannot be considered as quantitative.

Small-Angle X-ray Scattering (SAXS). Desmeared SAXS intensity profiles are shown in Figure 8 for the series of polyurethanes containing 30–80% by weight of hard segment. These profiles all exhibit a single scattering maximum or shoulder indicative of the hard-segment interdomain repeat distance. The interdomain repeat distances, d_{3D} and d_{1D}, may be calculated from these data either by application of Bragg's law equations or by correlation function analysis. Typical correlation functions for one of the polyurethanes are shown in Figure 9. The periodicity is estimated from the position of the first subsidiary maximum in these correlation functions.

The interdomain repeat distances estimated by both methods are presented in Table VI. Interpretation of the repeat distance for the PU-30 and PU-40 specimens is

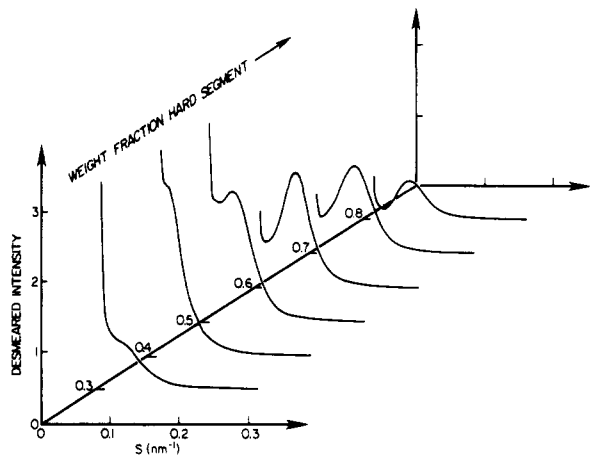

Figure 8. Desmeared SAXS intensity curves for the polyurethanes as a function of the hard-segment content.

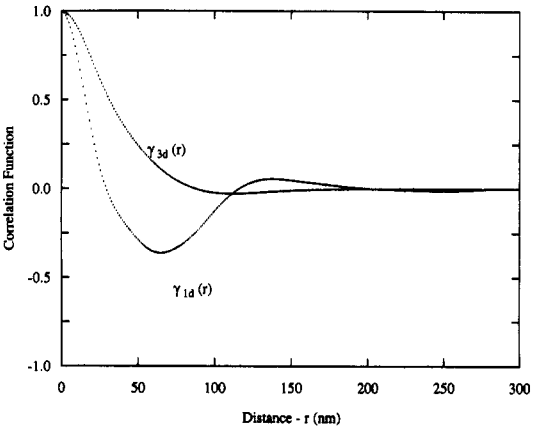

Figure 9. One-dimensional and three-dimensional experimental correlation functions for PU-50.

Table VI
Lamellar Repeat Distances (nm)

	d_{3D}		d_{1D}	
sample	from γ_{3D}	from Bragg's law	from γ_{1D}	from Bragg's law (Is^2)
PU-30	21.1		15.2	15.4
PU-40	28.3		21.9	22.0
PU-50	20.2	22.4	13.7	15.1
PU-60	18.4	17.2	13.3	14.4
PU-70	16.1	15.1	11.7	12.5
PU-80	16.2	15.0	11.8	12.3

complicated by the fact that the hard microdomain structure is discontinuous in these materials. It is not known whether the hard microdomain morphology of these specimens is disklike, spherical, cylindrical, or random. Knowledge of the microphase geometry is required if the repeat distance is to be properly interpreted.

Polyurethanes with hard-segment contents of 50% or higher have a continuous hard microdomain structure and may also have continuous soft microphases. There is substantial evidence that the microdomains in these latter materials are lamellar. The lamellar repeat distances (Table VI) for the higher hard-segment content polyurethanes show an inverse linear dependence on the hard-segment content. This behavior is inconsistent with hard-segment models invoking extended hard-segment configurations[1,2,11,55,56] since the average sequence length increases with hard-segment content.

The same qualitative trend in the lamellar repeat distance was found in our previous studies of these materials prepared by melt pressing above the order–disorder transition temperature.[6] The magnitudes of the

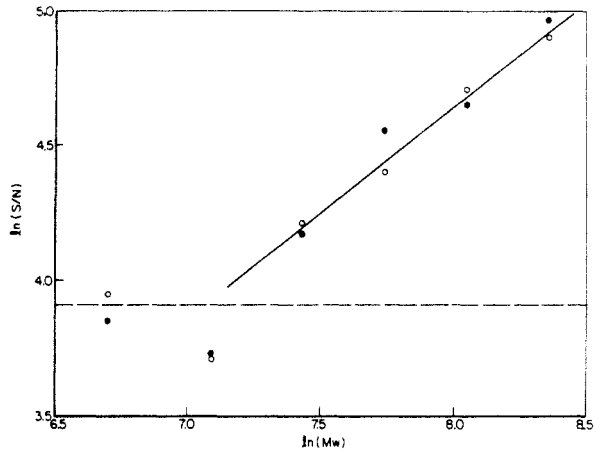

Figure 10. Specific interface area per hard-segment sequence as a function of the average hard-segment molecular weight (open circles). The dashed line denotes the prediction of the extended-chain model; the filled circles denote the lamellar model. The solid line is drawn with a slope of unity.

repeat distances in the present work are approximately 1 MDI repeat unit longer than those found for the melt-pressed materials. This observation is consistent with data in the preceding paper which indicate that the melting points and degree of crystallinity are higher in the compression-molded samples studied herein. This result not only shows that the morphology of polyurethanes is sensitive to thermal history but also provides additional evidence supporting the lamellar model. It is well-known for chain-folded semicrystalline homopolymers, for example, that crystal thickening is accompanied by an elevation in the melting point. A similar behavior is seen for the polyurethanes.[44]

A further test of the validity of the lamellar model is furnished by calculation of the interfacial area for each hard-segment sequence, S/N. S/N may be calculated by three separate means. The specific interface area per hard segment for an extended chain model is roughly independent of molecular weight, being equivalent to twice the effective cross-sectional area per chain,[6] or ca. 0.50 nm^2. For a lamellar system, S/N is given by[57]

$$S/N = 2(\nu_h + \nu_s)/d_{1D} \quad (13)$$

where ν is the volume per sequence of the hard (h) or soft (s) segment and is readily calculated from the mass densities.[42] The lamellar model has been used extensively to characterize diblock copolymer morphology. Its major assumptions are that both microphases are continuous and that there is no segmental intermixing. Finally, S/N can be estimated from the chain junction model,[6] which is based upon the concept of partial solubilization of hard segments below the critical length.[5]

Calculated S/N values from the lamellar and extended-chain models appear in Figure 10. The lamellar model data for specimens with continuous hard microdomains follow a linear dependence on molecular weight. This trend is self-consistent with the assumption of a lamellar model if the lamellar thickness is constant and is precisely what is expected from the Koberstein–Stein model. In the model, segments with the critical hard-segment sequence length form the core of the microdomain, with longer sequences folding or coiling back into the domain of critical thickness. As the sequences become longer, more chain folds must occur if the thickness is to remain constant. The increase in folding is directly proportional to the increase in molecular weight and causes a commensurate increase in the interfacial area per chain junction. It follows then, for lamellae of constant thickness, that S/N should scale linearly with the average hard-segment molecular weight, in agreement with the data.

Table VII
Interfacial Parameter Diffuse Boundary Thickness (nm)

sample	sigmoidal gradient σ	linear gradient E^a	S/V (m^2/cm^3)
PU-30	0.22 ± 0.03	0.73 ± 0.10	335 ± 4
PU-40	0.45 ± 0.10	1.56 ± 0.35	306 ± 21
PU-50	0.27 ± 0.04	0.94 ± 0.14	272 ± 18
PU-60	0.28 ± 0.04	0.97 ± 0.10	298 ± 20
PU-70	0.29 ± 0.02	1.00 ± 0.7	252 ± 8
PU-80	0.18 ± 0.03	0.62 ± 0.10	263 ± 9

[a] $E = 12^{1/2}\sigma$.

According to the chain junction model, S/N is related to the surface-to-volume ratio by

$$S/N = (S/V)/fX \quad (14)$$

where X is the overall number density of hard–soft-segment chain junctions, and f is the fraction of hard segments that are segregated into microdomains. The value of X is calculated[6] from the ideal hard-segment sequence distribution[58] assuming complete reaction. The parameter f depends upon the critical hard-segment sequence length for segregation and is used as an adjustable parameter.

The values of S/V required in (14) are determined by application of the modified Porod law relations [see (8)–(10)]. The resultant values of the interphase thickness parameter, σ, the linear gradient thickness, E, and S/V appear in Table VII. The S/V values are smaller than those reported for the melt-pressed materials.[6] Lower S/V values are expected, since the microdomain repeat distances are larger.

A larger lamellar thickness should also reduce the surface roughness and diffuse boundary thickness of the microdomains. A thicker microdomain requires dissolution of longer hard segments into the soft microphase. The sequences left segregated into the microdomains are then less heterogeneous in length and can pack more easily with a lower diffuse boundary thickness. The data in Table VII are consistent with this hypothesis, their magnitudes being roughly half of those determined previously[6] for melt-pressed specimens with continuous hard-segment microdomains. The diffuse boundary thickness for these specimens, incorporating hard-segment contents between 50 and 80%, is essentially constant, as would be expected for a folded or coiled chain hard-segment structure. The σ value increases from PU-30 to PU-40, behavior expected for an extended-chain, fringed micelle model, since the heterogeneity in the hard-segment sequence length increases with an increase in the hard-segment content for this model.

Experimental values of S/N can be calculated from the measured surface-to-volume ratios according to (14). An apparent critical hard-segment sequence length, N_c, can be obtained by adjusting the value in f in (14) until the S/N value matches that obtained from the lamellar model. Table VIII presents this comparison for specimens that show behavior characteristic of a continuous lamellar morphology. Column designations such as $N = 3$ signify that hard segments with N or fewer MDI residues are dissolved within the soft microphase (i.e., $N = N_c - 1$). A good correspondence between the two models is found for values of N between 2 and 3. The estimated critical length for microphase separation therefore is ca. 3–4 (i.e., 3–4 MDI residues). This estimate assumes complete conversion; the critical lengths would be higher if a lower conversion were assumed.

Table VIII
Specific Interfacial Area S/N (Å²)

sample	extended-chain model	lamellar model	chain junction model $N=1$	$N=2$	$N=3$
PU-30	50	52	29	47	75
PU-40	50	41	31	42	57
PU-50	50	67	43	53	65
PU-60	50	81	66	77	90
PU-70	50	110	83	93	104
PU-80	50	134	144	156	169

Table IX
Electron Density Variance Calculations

specimen	electron density variances [(mol e/cm³)² × 10⁻³] $\overline{\Delta\rho_c^2}$	$\overline{\Delta\rho^{2\prime}}$	$\overline{\Delta\rho^{2\prime\prime}}$	overall degree of microphase separation, $\overline{\Delta\rho^{2\prime\prime}}/\overline{\Delta\rho_c^2}$	fraction of mixing within interphase, f	fraction of mixing within microphase, $1-f$
PU-30	2.38	0.525	0.625	0.22	0.05	0.95
PU-40	2.85	0.625	0.792	0.24	0.08	0.92
PU-50	3.10	0.972	1.080	0.31	0.05	0.95
PU-60	3.10	1.030	1.170	0.33	0.07	0.93
PU-70	2.83	0.974	1.110	0.34	0.07	0.93
PU-80	2.20	0.583	0.649	0.27	0.04	0.96

The nature of intersegmental mixing can be further probed by determination of electron density variances according to (6), (11), and (12) and examination of the relationships amongst these quantities.[1,2] The ratio $\overline{\Delta\rho^{2\prime}}/\overline{\Delta\rho_c^{2\prime\prime}}$ is a measure of the overal degree of microphase separation. Its value is unity for an ideally separated material and is zero for complete mixing. The fraction of mixing that occurs within the diffuse interphase, f, is equal to

$$f = \frac{\overline{\Delta\rho^{2\prime\prime}} - \overline{\Delta\rho^{2\prime}}}{\overline{\Delta\rho^{2\prime\prime}} - \overline{\Delta\rho_c^2}} \tag{15}$$

It follows that the fraction of intersegmental mixing occurring within the microphases is $(1-f)$.

The results of electron density variance calculations are listed in Table IX. The overall degree of microphase separation increases with an increase in the hard-segment content, except for PU-80. This trend is expected if the hypothesis of a critical segment length is correct. Materials of higher hard-segment content have fewer segments below the critical length since their average segment length is longer. Consequently, the overall degree of phase separation generally improves as the hard-segment content increases. The results for PU-80 may reflect constraints in packing these long sequences in an ordered lamellar fashion that lead to additional mixing. Dissolution of unlike segments within the microphases constitutes the majority of intersegmental mixing, accounting for about 95% of the overall mixing. Interfacial mixing makes only a minor (ca. 5%) contribution to the mixing for these polyurethanes as processed.

Summary Discussion. The microdomain structure and thermomechanical properties have been characterized for a series of compression-molded MDI/BD/PPO–PEO segmented polyurethane block copolymers as a function of the overall hard-segment content. At high heating rates, the DSC thermograms exhibit only a single endotherm, suggesting that a single microdomain structure is manifest for each material. The results of wide-angle diffraction experiments are consistent with the predominance of the type I[39,49] or extended[40] crystal structure in the MDI/BDO hard segments. The degree of crystallinity of the hard segments reaches a maximum of ca. 22% for a polyurethane with a hard-segment content of 70%. At low heating rates, restructuring (i.e., melt recrystallization) can occur during the DSC scan, leading to the observance of multiple melting endotherms.

Thermomechanical and SAXS analyses indicate that a continuous hard microdomain structure is manifest for materials with a hard-segment content greater than 40–50%. Polyurethanes with 40% or less by weight of hard segment have a discrete hard microdomain structure; catastrophic flexure is found to be coincident with the soft microphase T_g detected by DSC experiments. It is difficult from these data to clearly assess their morphology; however, some results suggest that the domains may be of an extended-chain, fringed micellar nature. For compositions greater than this threshold, initial flexure does not occur until an apparent hard microdomain T_g is observed and catastrophic flexure does not occur until much higher temperatures (ca. 160 °C). In this range of compositions, the results correspond well to the concepts embodied in the Koberstein–Stein model for hard microdomain structure, showing properties consistent with a lamellar morphology.

Penetration probe results reflect a similar behavior. For materials with a discrete hard microdomain structure, initial softening is coincident with the apparent hard microdomain T_g. Materials with a continuous hard microdomain morphology, on the other hand, exhibit penetration probe position versus temperature profiles more characeteristic of expansion probe experiments. A distinct increase in the rate of expansion provides a further indication of an apparent hard microdomain glass transition temperature for these materials. In addition, catastrophic softening for materials of continuous hard microdomain morphology is coincident with the onset temperature of the first high-temperature endotherm, whereas softening occurs significantly below this temperature for compositions with discrete hard microdomains.

Apparent hard microdomain T_g's determined by penetration probe TMA correspond closely to the occurence of a small apparent endotherm in the DSC thermogram. The hard microdomain T_g's indicated by flexure probe TMA are lower by 10–25 °C from the values determined by the other techniques (due to a lower scan rate) but exhibit the same trend with composition. The apparent hard microdomain T_g decreases more or less monotonically as the hard-segment content increases, indicative of an augmentation in the amount of soft segment incorporated within the microdomain.

Soft microphase glass transition temperatures were determined by DSC and flexure probe TMA. For compositions below the hard-segment continuity threshold, the values furnished by the techniques are in good accord. For compositions above the threshold, the values indicated by TMA exceed significantly those values determined by DSC. The lowest soft microphase temperature is found for the polyurethane with a hard-segment content of 50%. This is consistent with our previous findings and interpretation[6] that the highest degree of microphase separation is attained for this composition since packing constraints for lamellar hard microdomains are a minimum when the fractions of the two microphases are equivalent. The soft microphase T_g's for materials with less than 40% hard segment correspond to the predictions of a modified Fox equation, assuming a completely homogeneous morphology. The microdomain structure is therefore at best poorly developed in these materials.

The ΔC_p at the soft microphase T_g decreases linearly with an increase in the hard-segment content but falls below the theoretical value, indicating that some of the

soft-segment material is resident within the hard segment. The deviation from the ideal value increases with increasing hard segment, consistent with the corresponding decrease in the apparent hard microdomain T_g.

SAXS results support the concept of a critical hard-segment sequence length, below which hard segments remain dissolved within the soft microphase. The apparent lamellar repeat distance and the interfacial thickness of these materials are insensitive to changes in the hard-segment content. The specific interface area is found to scale directly with molecular weight (i.e., average hard-segment length), as expected for a model of coiled or folded chain lamellae. The degree of microphase separation generally increases with the hard-segment content, correlating well with the associated decrease in the fraction of hard-segment sequences below the critical length. The majority of intersegmental mixing (ca. 95%) occurs by dissolution of unlike sequences into the microphases. Only a minor portion (ca. 5%) of the mixing occurs within the interphases. Comparisons of the measured specific interfacial areas with calculations based upon a chain junction model suggest that the critical hard-segment sequence length contains 3–4 MDI residues. In the paper that follows, these X-ray and thermal analysis data are combined in order to estimate microphase compositions and further test the validity of the lamellar microdomain model.

Acknowledgment. The portion of this work carried out by L.M.L. was supported by National Science Foundation Grant DMR-81054612 provided by the Polymers Program of the Division of Materials Research. J.T.K. and A.F.G. acknowledge partial support by the Office of Naval Research. Much of this work was performed while the authors were associated with Princeton University, using thermal analysis equipment that was procured through NSF Grant DMR-8206187. We gratefully acknowledge Dr. J. A. Emerson for his assistance in this work and for making the X-ray camera available for our use. Finally, we thank Dr. R. J. Zdrahala, formerly of Union Carbide Corp., for supplying the materials.

References and Notes

(1) Bonart, R.; Müller, E. H. *J. Macromol. Sci., Phys.* **1974**, *B10*, 177.
(2) Bonart, R.; Müller, E. H. *J. Macromol. Sci., Phys.* **1974**, *B10*, 345.
(3) Schneider, N. S.; Desper, C. R.; Illinger, J. L.; King, A. O.; Barr, D. *J. Macromol. Sci., Phys.* **1975**, *B11*, 527.
(4) Van Bogart, J. W.; Gibson, P. E.; Cooper, S. L. *J. Polym. Sci., Polym. Phys. Ed.* **1983**, *21*, 65.
(5) Koberstein, J. T.; Stein, R. S. *J. Polym. Sci., Polym. Phys. Ed.* **1983**, *21*, 1439.
(6) Leung, L. M.; Koberstein, J. T. *J. Polym. Sci., Polym. Phys. Ed.* **1985**, *23*, 1883.
(7) Abouzahr, S.; Wilkes, G. L.; Ophir, Z. *Polymer* **1982**, *23*, 1077.
(8) Ophir, Z.; Wilkes, G. L. *J. Polym. Sci., Polym. Phys. Ed.* **1980**, *18*, 1469.
(9) Bonart, R. *J. Macromol. Sci., Phys.* **1968**, *B2* (1), 115.
(10) Bonart, R.; Morbitzer, L.; Hentze, G. *J. Macromol. Sci., Phys.* **1969**, *B3* (2), 337.
(11) Bonart, R.; Morbitzer, L.; Müller, E. H. *J. Macromol. Sci., Phys.* **1974**, *B9* (3), 447.
(12) Blackwell, J.; Gardner, H. *Polymer* **1979**, *20*, 13.
(13) Blackwell, J.; Nagarajan, M. *Polymer* **1981**, *22*, 202.
(14) Huh, D. S.; Cooper, S. L. *Polym. Eng. Sci.* **1971**, *11*, 369.
(15) Koberstein, J. T. Ph.D. Dissertation, University of Massachusetts, Amherst, MA, 1979.
(16) Seymour, R.; Cooper, S. L. *J. Polym. Sci., Polym. Lett.* **1971**, *9*, 689.
(17) Samuels, S.; Wilkes, G. *J. Polym. Sci., Polym. Phys. Ed.* **1973**, *11*, 807.
(18) Jacques, C. *Polymer Alloys, Blends, Blocks, Grafts, and Interpenetrating Networks*; Klempner, D., Frisch, K., Eds.; Plenum Press: New York, 1977.
(19) Senich, G. A.; MacKnight, W. J. *Adv. Chem. Ser.* **1979**, *176*, 97.
(20) Brunette, C. M.; Hsu, S. L.; MacKnight, W. J.; Schneider, N. S. *Polym. Eng. Sci.* **1981**, *21*, 163.
(21) Huh, D. S.; Cooper, S. L. *Polym. Eng. Sci.* **1971**, *11*, 369.
(22) Ng, H.; Allegrezza, A. E.; Seymour, R. W.; Cooper, S. L. *Polymer* **1973**, *14*, 255.
(23) Illinger, J. I.; Schneider, N. S.; Karasz, F. E. *Polym. Eng. Sci.* **1972**, *12*, 25.
(24) Zdrahala, R. J.; Critchfield, F. E.; Gerkin, R. M.; Hager, S. L. *J. Elastomers Plast.* **1980**, *12*, 184.
(25) Kajiyama, T.; MacKnight, W. J. *Macromolecules* **1969**, *2*, 254.
(26) Kajiyama, T.; MacKnight, W. J. *J. Trans. Soc. Rheol.* **1969**, *13* (4), 527.
(27) Seymour, R. W.; Cooper, S. L. *Macromolecules* **1973**, *6*, 48.
(28) Hesketh, T. R.; Van Bogart, J. W. C.; Cooper, S. L. *Polym. Eng. Sci.* **1980**, *20*, 190.
(29) Schneider, N. S.; Paik Sung, C. S.; Matton, R. W.; Illinger, J. L. *Macromolecules* **1975**, *8*, 62.
(30) Van Bogart, J. W. C.; Bluemke, D. A.; Cooper, S. L. *Polymer* **1981**, *22*, 1428.
(31) Schneider, N. S.; Paik Sung, C. S. *J. Polym. Sci., Polym. Chem. Ed.* **1977**, *17*, 73.
(32) Camberlin, Y.; Pascault, J. P. *J. Polym. Sci., Polym. Chem. Ed.* **1983**, *21*, 415.
(33) Koberstein, J. T.; Russell, T. P. *Macromolecules* **1986**, *19*, 714.
(34) Leung, L. M.; Koberstein, J. T. *Macromolecules* **1986**, *19*, 706.
(35) Dumais, J. J.; Jelinski, L. W.; Leung, L. M.; Gancarz, I.; Galambos, A.; Koberstein, J. T. *Macromolecules* **1985**, *18*, 116.
(36) Kintantar, A.; Jelinski, L. W.; Gancarz, I.; Koberstein, J. T. *Macromolecules* **1986**, *19*, 1876.
(37) Koberstein, J. T.; Gancarz, I.; Clarke, T. C. *J. Polym. Sci., Polym. Phys. Ed.* **1986**, *24*, 2487.
(38) Camberlin, Y.; Pascault, J. P.; Letoffe, M.; Claudy, P. *J. Polym. Sci., Polym. Chem. Ed.* **1982**, *20*, 383.
(39) Briber, R. M.; Thomas, E. L. *J. Macromol. Sci., Phys.* **1983**, *B22* (4), 509.
(40) Blackwell, J.; Lee, C. D. *J. Polym. Sci., Polym. Phys. Ed.* **1984**, *22*, 759.
(41) Macosko, C. W., private communication.
(42) Leung, L. M. Ph.D. Dissertation, Princeton University, Princeton, NJ, 1985.
(43) Vonk, C. G. *J. Appl. Crystallogr.* **1973**, *6*, 81.
(44) Galambos, A. F. PhD Dissertation, Princeton University, Princeton, NJ, 1989.
(45) Koberstein, J. T.; Morra, B.; Stein, R. S. *J. Appl. Crystallogr.* **1980**, *13*, 34.
(46) Koberstein, J. T.; Stein, R. S. *J. Polym. Sci., Polym. Phys. Ed.* **1983**, *21*, 2181.
(47) Ruland, W. *J. Appl. Crystallogr.* **1971**, *4*, 70.
(48) Wood, L. A. *J. Polym. Sci.* **1958**, *28*, 319.
(49) Fox, T. G. *Bull. Am. Phys. Soc.* **1956**, *50*, 549.
(50) Koberstein, J. T.; Galambos, A. F., to be published in *Macromolecules*.
(51) Cohen, R. E.; Ramos, A. R. *Macromolecules* **1979**, *12*, 131.
(52) Briber, R. M.; Thomas, E. L. *J. Polym. Sci., Polym. Phys. Ed.* **1985**, *23*, 1915.
(53) Born, L.; Crone, J.; Hespe, H.; Müller, E. H.; Wolf, K. H. *J. Polym. Sci., Polym. Phys. Ed.* **1984**, *22*, 163.
(54) Alexander, L. E. *X-Ray Diffraction Methods in Polymer Science*; Wiley-Interscience: New York, 1969.
(55) Eisenbach, C. D.; Hayen, H.; Nefzger, H. *Makromol. Chem., Rapid Commun.* **1989**, *10*, 463.
(56) Blackwell, J.; Lee, C. D. L. *J. Polym. Sci., Polym. Phys. Ed.* **1983**, *21*, 2169.
(57) Hashimoto, T.; Shibayama, M.; Kawai, H. *Macomolecules* **1980**, *13*, 1237.
(58) Peebles, L. H. *Macromolecules* **1974**, *7*, 872; **1976**, *9*, 58.

Registry No. (BDO)(MDI)(PPO)(PEO) (block copolymer), 143495-43-6.